

VLT/X-shooter spectroscopy of the afterglow of GRB 130606A[★]

Chemical abundances and reionisation at $z \sim 6$

O. E. Hartoog¹, D. Malesani², J. P. U. Fynbo², T. Goto^{2,3}, T. Krühler^{2,4}, P. M. Vreeswijk⁵, A. De Cia⁵, D. Xu², P. Møller⁶, S. Covino⁷, V. D’Elia^{8,9}, H. Flores¹⁰, P. Goldoni¹¹, J. Hjorth², P. Jakobsson¹², J.-K. Krogager^{2,4}, L. Kaper¹, C. Ledoux⁴, A. J. Levan¹³, B. Milvang-Jensen², J. Sollerman¹⁴, M. Sparre², G. Tagliaferri⁷, N. R. Tanvir¹⁵, A. de Ugarte Postigo^{16,2}, S. D. Vergani¹⁰, K. Wiersema¹⁵, J. Datson¹⁷, R. Salinas^{18,19}, K. Mikkelsen²⁰, and N. Aghanim²¹

(Affiliations can be found after the references)

Received ...; accepted, 2014

ABSTRACT

Context. The reionisation of the universe is a process that is thought to have ended around $z \sim 6$, as inferred from spectroscopy of distant bright background sources such as quasars (QSO) and gamma-ray burst (GRB) afterglows. Furthermore, spectroscopy of a GRB afterglow provides insight in its host galaxy, which is often too dim and distant to study otherwise.

Aims. For GRB 130606A at $z = 5.913$ we have obtained a high S/N spectrum covering the full optical and near-IR wavelength region at intermediate spectral resolution with VLT/X-shooter. We aim to measure the degree of ionisation of the IGM between $z = 5.02 - 5.84$, and to study the chemical abundance pattern and dust content of its host galaxy.

Methods. We estimate the UV continuum of the GRB afterglow using a power-law extrapolation, then measure the flux decrement due to absorption at $\text{Ly}\alpha$, β and γ wavelength regions. Furthermore, we fit the shape of the red damping wing of $\text{Ly}\alpha$. The hydrogen and metal absorption lines formed in the host galaxy are fitted with Voigt profiles to obtain column densities. We investigate whether ionisation corrections need to be applied.

Results. Our measurements of the $\text{Ly}\alpha$ -forest optical depth are consistent with previous measurements of QSOs, but have much smaller uncertainty than these. The red-damping-wing analysis yields a neutral fraction $x_{\text{H I}} < 0.03$ (3σ). We obtain column density measurements of H, Al, Si, and Fe; for C, O, S and Ni we obtain limits. The ionisation due to the GRB is estimated to be negligible (corrections < 0.03 dex), but larger corrections may apply due to pre-existing radiation field (up to 0.3 dex based on sub-DLA studies). Assuming that $[\text{Si}/\text{Fe}] = +0.79 \pm 0.13$ is due to dust depletion, the dust-to-metals ratio is similar to the Local Group value.

Conclusions. Our measurements confirm that the Universe is already predominantly ionised over the redshift range probed in this work, but was slightly more neutral at $z > 5.6$. GRBs are useful probes of the IGM ionisation state of the early Universe, but because of internal scatter we need a larger statistical sample to draw robust conclusions. The high $[\text{Si}/\text{Fe}]$ in the host can be due to dust depletion, α -element enhancement or a combination. The very high value of $[\text{Al}/\text{Fe}] = 2.40 \pm 0.78$ might be due to a proton capture process and is probably connected to the stellar population history. We estimate the host metallicity to be $-1.5 < [\text{M}/\text{H}] < -1.2$ (3% – 6% of solar).

Key words. Gamma-ray bursts: individual: GRB 130606A, Cosmology: observations, Cosmology: dark ages, reionisation, first stars, ISM: abundances

1. Introduction

The potential of gamma-ray bursts (GRBs) as probes of star formation and the physics of the inter-galactic medium (IGM) back to the epoch of the first galaxies was appreciated very early in

the so-called afterglow era (e.g., Wijers et al. 1998; Lamb & Reichart 2000; Ciardi & Loeb 2000). This promise has been bolstered by the rapid increase in the highest recorded spectroscopic redshift for GRBs from $z = 4.5$ in 2000 to $z = 8.2$ in 2009 (Andersen et al. 2000; Tanvir et al. 2009; Salvaterra et al. 2009). There are three main objectives in using GRBs to probe star formation and the IGM at high redshifts: to measure chemical abundances in very “primitive” conditions (e.g., dominated by Population III stars, Price et al. 2007; Wang et al. 2012; Sparre et al. 2014), to measure the neutral fraction of the IGM from the shape of the red damping wing (e.g., Miralda-Escudé 1998; Totani et al. 2006; Xu & Wei 2009; Greiner et al. 2009; Patel et al. 2010), and to pinpoint locations of star formation (Berger et al. 2007; Ruiz-Velasco et al. 2007; Tanvir et al. 2012). The last objective advances with each new detection, but especially for the first two objectives the full potential is still far from realised.

[★] Based on observations carried out under prog. ID 091.C-0934(C) with the X-shooter spectrograph installed at the Cassegrain focus of the Very Large Telescope (VLT), Unit 2 – Kueyen, operated by the European Southern Observatory (ESO) on Cerro Paranal, Chile. Partly based on observations made with the Nordic Optical Telescope, operated on the island of La Palma jointly by Denmark, Finland, Iceland, Norway, and Sweden, in the Spanish Observatorio del Roque de los Muchachos of the Instituto de Astrofísica de Canarias. Partly based on observations made with the Italian Telescopio Nazionale Galileo (TNG) operated on the island of La Palma by the Fundación Galileo Galilei of the INAF (Istituto Nazionale di Astrofisica) at the Spanish Observatorio del Roque de los Muchachos of the Instituto de Astrofísica de Canarias, under programme A26TAC_63.

GRB afterglows can be extremely bright, but also fade very rapidly. In order to obtain high-quality spectra, rapid follow-up at the largest optical telescopes is required. Primarily thanks to the *Swift* mission (Gehrels et al. 2004), studying the high-redshift universe through GRB afterglows has progressed well over the last years (e.g., Kawai et al. 2006; Price et al. 2007; Ruiz-Velasco et al. 2007; Thöne et al. 2013; Sparre et al. 2014). Traditionally, high-redshift galaxies are selected as Lyman-break galaxies (LBGs, Giavalisco 2002; Steidel et al. 2003), Ly α emitters (Stark et al. 2010; Ono et al. 2012; Pentericci et al. 2014) and damped Ly α absorbers towards quasars (QSO-DLAs, Wolfe et al. 2005). GRB host galaxies studied in absorption through afterglows (sometimes referred to as GRB-DLAs) are analysed using similar methods as those applied to QSO-DLAs, but intrinsic and observational biases are very different between these two classes of objects (see e.g. Prochaska et al. 2007a; Fynbo et al. 2008). Contrary to e.g. LBGs, GRB host galaxies are not selected by their brightness, which provides the opportunity to explore a different range of luminosities and therefore sizes and masses of high-redshift galaxies.

In this paper we present spectroscopic observations of the afterglow of the $z = 5.913$ GRB 130606A obtained with X-shooter on the European Southern Observatory (ESO) Very Large Telescope (VLT). The objective of the paper is to address the issues of chemical abundances in the host galaxy and the ionisation state of the IGM. Independent analyses of this event, though using data at significantly lower spectral resolution and with smaller wavelength coverage, can be found in Chornock et al. (2013), Castro-Tirado et al. (2013a) and Totani et al. (2014). Our results are discussed in the context of the results from these earlier reports. The superior resolution and wavelength range we achieve with the data presented here, with the associated ability to perform direct line fits for abundances, provide the motivation for this paper.

For the cosmological calculations we assume a Λ CDM universe with $\Omega_{\Lambda} = 0.73$, $\Omega_{\text{m}} = 0.27$, and $H_0 = 71 \text{ km s}^{-1} \text{ Mpc}^{-1}$ from the *Wilkinson Microwave Anisotropy Probe* (WMAP) seven-year data (Komatsu et al. 2011). Magnitudes are in the AB system. Column densities are given as $\log(N/\text{cm}^{-2})$. We use 1σ error bars unless explicitly noted otherwise.

2. Observations

GRB 130606A was detected by *Swift* on June 6 at 21:04:39 UT (Ukwatta et al. 2013). The burst was relatively long with a T_{90} duration of $277 \pm 19 \text{ s}$ (Barthelmy et al. 2013).

We first observed the field of GRB 130606A with the Nordic Optical Telescope (NOT) equipped with the MOsaic CAmera (MOSCA) in the r -band ($3 \times 200 \text{ s}$). See Table 1 for a log of the observations, including those obtained with the Telescopio Nazionale Galileo (TNG). Observations started at 20:35 UT or 0.5 hr after the GRB trigger (Ukwatta et al. 2013; Xu et al. 2013b). Consistent with the *Swift*/XRT position (Osborne et al. 2013) we detected a new source with an r -band magnitude of 20.8 mag at RA (J2000) = $16^{\text{h}}37^{\text{m}}35.188^{\text{s}}$, Dec (J2000) = $+29^{\circ}47'47.03''$ (Xu et al. 2013b). The source coincided with the one reported by Jelinek et al. (2013). Observations in the near-infrared revealed that the afterglow was extremely bright ($K_s = 15.0$ about half an hour after the burst; Nagayama 2013a,b). We observed the field again 3 hr later with NOT/MOSCA in the r and i -bands. In Figure 1 we show our i -band image compared to a pre-explosion image from the Sloan Digital Sky Survey. It soon became clear through spectroscopy and multi-band photometry at a number of telescopes

Table 1. Top: of of the NOT and TNG observations with (1) mid-time of observations (2) time since the burst (3) exposure time (4) seeing (5) filter and (6) measured magnitude. Bottom: main parameters of the VLT/X-shooter observations, frame by frame, with (1) mid-time, (2) exposure time, (3) average airmass, (4) average seeing measured in the VIS and NIR 2D spectra. The last line contains the average values for the VLT/X-shooter observations.

NOT and TNG					
Mid-time UTC	T_{GRB} (day)	Exptime (s)	Seeing (")	Filter	Magnitude (AB mag)
June 6.89179	0.01356	30	1.6	NOT/ r	20.51 ± 0.06
June 6.89434	0.01611	30	1.6	NOT/ r	20.79 ± 0.06
June 6.89727	0.01904	300	1.6	NOT/ r	20.90 ± 0.03
June 6.90137	0.02314	300	1.8	NOT/ r	21.19 ± 0.04
June 7.02835	0.15012	300	1.1	NOT/ i	19.83 ± 0.03
June 7.03241	0.15418	300	1.1	NOT/ r	22.93 ± 0.08
June 7.90616	1.02793	5×300	0.7	NOT/ z	21.02 ± 0.03
June 7.92510	1.04687	4×300	0.7	NOT/ i	23.37 ± 0.08
June 8.15646	1.27823	7×180	1.1	TNG/ i	23.99 ± 0.14
June 8.17616	1.29793	7×180	1.1	TNG/ z	21.50 ± 0.04
June 10.1230	3.24474	3×600	0.8	TNG/ z	22.26 ± 0.14
June 12.0047	5.12648	8×300	0.6	NOT/ z	> 22.70

VLT/X-shooter				
Mid-time UTC	T_{GRB} (day)	Exptime (s)	Airmass	Seeing (")
June 7.17990	0.30167	600	1.72	1.2 - 0.9
June 7.18809	0.30986	600	1.72	1.2 - 0.9
June 7.19899	0.32076	600	1.73	1.2 - 0.9
June 7.20707	0.32884	600	1.74	1.2 - 1.0
June 7.23147	0.35324	600	1.77	1.4 - 1.2
June 7.23955	0.36132	600	1.88	1.1 - 0.9
Average values				
June 7.20751	0.32928	600	1.76	1.22 - 0.97

that GRB 130606A was a very distant GRB (Castro-Tirado et al. 2013b; Lunnan et al. 2013; Afonso et al. 2013). We subsequently acquired a medium resolution spectrum with the X-shooter spectrograph mounted at the ESO/VLT (Vernet et al. 2011), using nodding mode with 1×2 binning (i.e., binning in the dispersion direction, Xu et al. 2013a). Because we used a K -band blocking filter to increase the signal-to-noise ratio (S/N) at shorter near-IR wavelengths, the spectral coverage extends from 3000 to about 20 000 Å, corresponding to 430 – 2900 Å in the GRB rest frame. Observation started at 03:57:41 UT on 7 June, 2013 (see Table 1). Given that the atmospheric dispersion corrector was not working at the time of the observation, we aligned the slit according to the parallactic angle and spread the observation over three observing blocks (OBs) of each $2 \times 600 \text{ s}$ in the UVB, VIS and NIR arm, respectively. After each OB, we reset the position angle to the new parallactic angle to minimise flux losses in the UVB and VIS arm. The mid exposure time is 7.829 hr post burst (Xu et al. 2013a). The slit widths were matched to the seeing conditions, i.e. we chose a $1''.0$, $0''.9$, and $0''.9$ slit in the UVB, VIS, and NIR arm, respectively. For this given instrument setup, the nominal resolving power $R = \lambda/\Delta\lambda$ is 5100, 8800, and 5300 in the UVB, VIS and NIR, respectively. For the VIS and NIR spectra we could directly measure the resolving power from the width of telluric absorption lines and find it to be 8700 and 6200, respectively. The NIR resolving power is higher than the nominal one because during most of the observations the seeing in this wavelength range was smaller than the slit width. The UVB spectrum shows no afterglow signal, as expected, given that the coverage of this arm falls below the Lyman break at the redshift

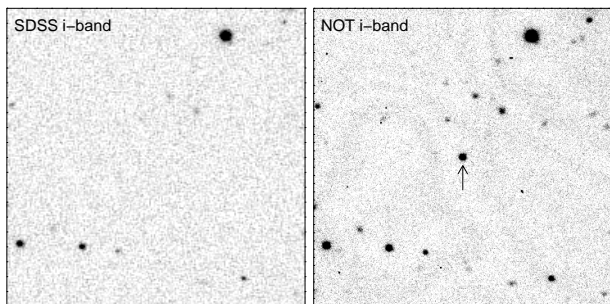


Fig. 1. The $80'' \times 80''$ field around the position of GRB 130606A in the i -band. The left panel shows a pre-explosion image from the Sloan Digital Sky Survey and the right panel our i -band image obtained with the NOT 3.5 hr after the burst. North is up and East is to the left.

of the GRB, and is not discussed further in the remainder of this paper.

VLT/X-shooter data were reduced with the X-shooter Pipeline version 2.2.0¹ (Goldoni 2011). The wavelength binning was chosen to be $0.2 \text{ \AA}/\text{px}$ in the VIS, and $0.6 \text{ \AA}/\text{px}$ in the NIR. All spectra were flux calibrated with the spectrophotometric standard star LTT3218. We transformed the wavelength solution to vacuum, and to the heliocentric frame. We corrected the VIS and NIR spectra for telluric absorption using the spectra of the telluric standard Hip095400 observed just after the afterglow with the same slit width and at a similar airmass. The telluric corrections built with those spectra were applied with the SPEXTOOL software (Vacca et al. 2003). This corrected version was only used for line measurements in contaminated regions, because in unaffected regions, the uncorrected results showed a slightly higher S/N.

3. Results

3.1. Astrometry

Based on the i -band image shown in Figure 1 we determine the position of the afterglow of RA(J2000) = 16:37:35.143, Dec(J2000) = +29:47:46.62 calibrated to the USNO-A2.0 catalog (Monet et al. 1998). The estimated error on the absolute position is $0.3''$ (Deutsch 1999). The position relative to stars in the field is much more precise with an uncertainty of about $0.05''$.

3.2. SED fitting

We construct a broad-band spectral energy distribution (SED) for the afterglow of GRB 130606A spanning the wavelength range from the NIR K -band to the X-ray energy range. Here, we follow the methodology outlined in Krühler et al. (2011) and use the X-shooter spectroscopy, photometric data from the Gamma-Ray Burst Optical/Near-Infrared Detector (GROND) as given in Afonso et al. (2013) and public X-ray data from the *Swift*/X-Ray Telescope (XRT) repository (Evans et al. 2007, 2009). We correct for the Galactic foreground extinction of $A_{V,\text{Gal}} = 0.08$ (Schlegel et al. 1998; Schlafly & Finkbeiner 2011).

After scaling the NIR spectroscopy to the photometry (data bluewards of $\text{Ly}\alpha$ are not fitted) to account for slit-losses and different observing times, the complete data set is well described with a single power-law continuum $F_\nu \propto \nu^{-\beta}$ with index $\beta = 1.02 \pm 0.03$, without evidence for reddening towards the GRB in addition to the Galactic component (see Figure 2).

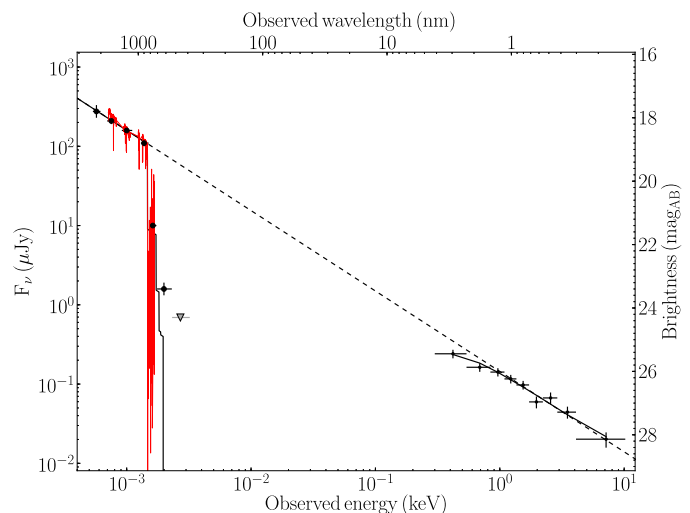


Fig. 2. The afterglow spectral energy distribution. The red spectrum is the X-shooter spectrum, the filled circles on the left are the GROND photometric points (Afonso et al. 2013) and the data points on the right are the (binned) *Swift*/XRT points. The solid line is the synchrotron spectrum with interstellar absorption, while the dashed line shows the unabsorbed synchrotron spectrum with best fit $\beta = 1.02$.

We set a 3σ upper limit of $A_V < 0.2 \text{ mag}$ at $\sim z_{\text{GRB}}$ assuming local extinction laws from the SMC, LMC or MW (Pei 1992). The intrinsic X-ray absorption is also consistent with zero; given the GRB's high redshift we obtain a 3σ upper limit of $N_{\text{H}}^X < 3 \times 10^{22} \text{ cm}^{-2}$.

3.3. Analysis of the red damping wing

We use the SED obtained in Section 3.2 to normalise the spectrum. The normalisation is generally much more secure for GRB afterglows, which are intrinsically simple power-laws (pure synchrotron emission), compared to the more complex spectra of QSOs. To constrain the ionisation state of the IGM we follow Miralda-Escudé (1998) and Totani et al. (2006) and make a joint fit of the hydrogen column density in the GRB host galaxy, $\log N_{\text{H I}}$, and the neutral fraction of the IGM, $x_{\text{H I}}$. In this analysis we assume a constant neutral fraction $x_{\text{H I}}$ between $z = 5.8$ (the results are not very sensitive to this value) and $z = 5.91248$, the redshift of the GRB that follows from fitting a Voigt profile to the $\text{Ly}\alpha$ absorption line (see Section 3.4 and Table 2). Each model specified by $\log N_{\text{H I}}$ and $x_{\text{H I}}$ is normalised to the observed spectrum at 8730 \AA . The χ^2 sum is calculated over the region 0 to 2000 km s^{-1} with respect to $\text{Ly}\alpha$. We perform the fit for three different slopes of the underlying afterglow continuum, $\beta = 0.96, 1.02, 1.08$ corresponding to the $\pm 2\sigma$ allowed region for the spectral slope (Section 3.2). The minimum χ^2 is reached for a fit with $x_{\text{H I}} = 0$ ($x_{\text{H I}} < 0.03$ at 3σ significance) and $\log N_{\text{H I}} = 19.94 \pm 0.01$. The best fit to the $\text{Ly}\alpha$ red wing can be inspected in Figure 3 and the $1, 2$ and 3σ confidence regions in Figure 4.

3.4. Metal absorption lines

In Figures A.1 and A.2 we show the afterglow spectrum redwards of the $\text{Ly}\alpha$ absorption line at 8400 \AA up to 18000 \AA , which marks the end of the H -band. The spectrum has a relatively high S/N (~ 20 per 0.2 \AA pixel in VIS redwards of $\text{Ly}\alpha$; ~ 10 per 0.6 \AA pixel in NIR), and many metal absorption lines are de-

¹ <http://www.eso.org/sci/software/pipelines/>

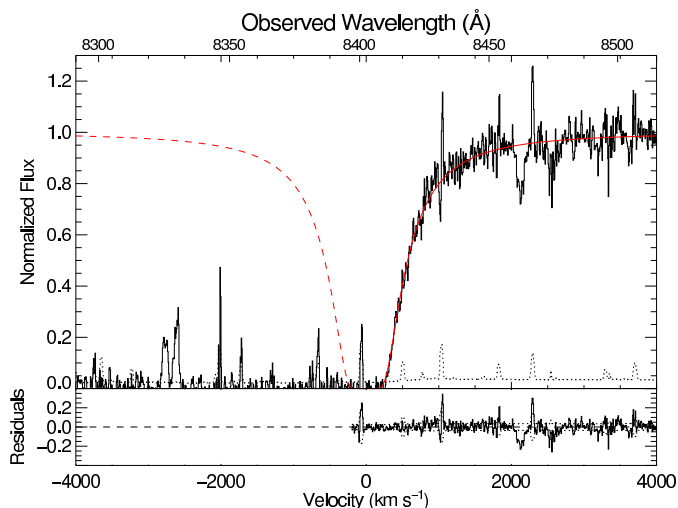


Fig. 3. The top panel shows spectral region around the Ly α feature with our best fit to the red wing overplotted in red. The model consists of a fully ionised intergalactic medium and a column density in the GRB host of $\log N_{\text{H I}} = 19.94 \pm 0.01$. The 1σ noise is plotted as a dotted line. The bottom panel shows the residuals from the fit with the $\pm 1\sigma$ region marked with a dotted line. The skyline residual in the bottom of the Ly α line should not be interpreted as Ly α emission.

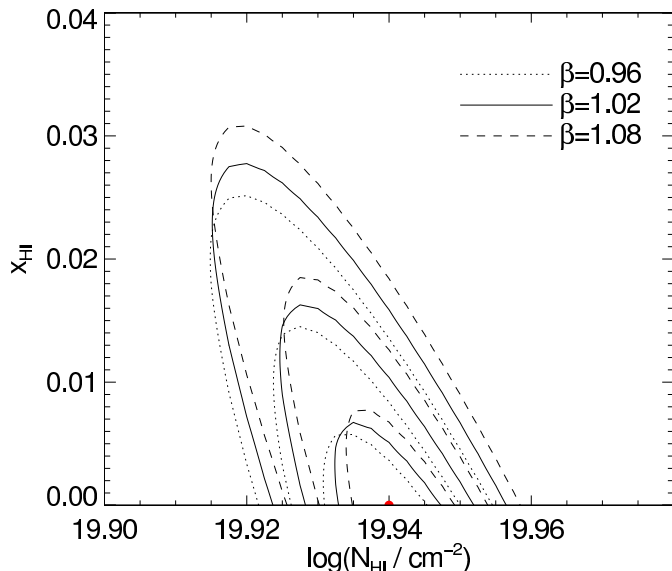


Fig. 4. 1, 2 and 3σ contours for a joint fit of the neutral hydrogen column density in the host galaxy, $\log N_{\text{H I}}$, and the neutral fraction of the intergalactic medium, $x_{\text{H I}}$. The fit has been performed for 3 different normalising power-law SEDs: $\beta = 0.96$, $\beta = 1.02$ (best fit), and $\beta = 1.08$. The red dot marks where the peak likelihood is reached.

tected. Most of these are from the host galaxy, but there is a number of intervening absorbers, see Section 3.5.

To determine the host-galaxy metal abundances we proceeded with Voigt-profile fits to the metal lines around $z = 5.913$, with VPFIT version 10.0². A Voigt-profile fit to the red wing of the Ly α absorption lines results in $\log N_{\text{H I}} = 19.925 \pm 0.019$; the blue wing is not visible due to ionisation in the IGM (see Section 3.6). This is consistent with the value from the combined fit for $\log N_{\text{H I}}$ and $x_{\text{H I}}$ (Section 3.3); for the remainder of this analysis we adopt $\log N_{\text{H I}} = 19.94 \pm 0.01$. Following the $\log N_{\text{H I}}$ distinctions for QSO absorbers, this system is formally a sub-

DLA, but only a factor of two below the DLA threshold (e.g., Wolfe et al. 2005).

We detect metal absorption lines of both low and high ionisation. We assume that the redshift z and Doppler parameter b of a specific velocity component is the same for all metal lines of neutral, singly and doubly ionised species. This assumption is commonly made for absorption spectra at intermediate spectral resolution. The z and b of components in the N v lines are not constrained to be the same as those of the low-ionisation species, because these species are expected to reside in different locations (see Section 3.4.1). The resulting Voigt-profile fits are shown in Figure 5. C iv and Si iv are not included in the overall fit with free z and b due to their strong saturation, but we have assumed the same velocity structure as N v, and left the column densities free to fit. They are shown for completeness. Table 2 shows the redshifts and b parameters of the Ly α line and the components of the metal lines that follow from the fits. Because the values of b indicate that the velocity broadening is mostly due to turbulent motion of the gas, and not due to temperature, we do not weight the b values with the ion mass. In fitting the ensemble of lines we also include undetected lines, as long as they are in regions without strong telluric contamination, in order to constrain the b values, and reduce the effect of (hidden) saturation. We have taken into account contributions from intervening absorbers, for details on these see Section 3.5.

Table 3 shows the resulting column densities for several ion species and states, per component, total, and in the metallicity notation $[X/H] \equiv \log(N(X)/N(H))_{\text{GRB}} - \log(n(X)/n(H))_{\odot}$ based on the total column density, and using reference solar abundances n from Asplund et al. (2009) following the recommendations by Lodders et al. (2009). These numbers are not corrected for ionisation or dust-depletion effects; see respectively Sections 3.4.3 and 3.4.4.

3.4.1. Kinematic structure of absorption lines

Table 2 gives the redshifts and b parameters of the three components of low- (2, 4, 5) and high-ionisation lines (1, 3, 6), and their relative velocity. In C ii, Si ii and Fe ii lines we find that component 4 is stronger than 5, while this is opposite in Al ii and Al iii, which show structures that are very similar to one another. N v shows a very different structure, which is broader, and where the absorption is strongest at highest relative velocities. The N v lines are not significantly affected by lines from intervening absorbers (see Section 3.5). High-ionisation lines such as N v are common in GRB afterglow spectra (see e.g., Fox et al. 2008). Prochaska et al. (2008) find that 6 out of 7 GRB afterglow spectra show N v absorption, and the majority has $N(\text{N v}) \geq 10^{14} \text{ cm}^{-2}$; for GRB 130606A we find $\log(N(\text{N v})/\text{cm}^{-2}) = 14.59 \pm 0.03$. However, in GRB afterglow spectra, these features are usually kinematically "cold": the lines are narrow and have velocity offsets $\delta v \lesssim 20 \text{ km s}^{-1}$ with respect to where the neutral gas is located. Our resolution is not high enough to make strong statements about the width of the lines but we do see a much larger offset: $\delta v \gtrsim 60 \text{ km s}^{-1}$ for the bulk of the N v absorption. In QSO-DLAs the detection rate of N v is much lower, and the lines are weaker (Fox et al. 2007; Prochaska et al. 2007b).

The velocity width of optically thin lines, ΔV , is sensitive to the mass of the host galaxy; therefore, together with the metallicity of the gas, it can be used to explore the evolution of the mass-metallicity (MZ) relation of galaxies from high redshifts to the local universe (e.g., Ledoux et al. 2006). In a recent study, Møller et al. (2013) found that the redshift evolution of the MZ relation for QSO-DLAs is flat in the early universe but that

² <http://www.ast.cam.ac.uk/~rfc/vpfit.html>

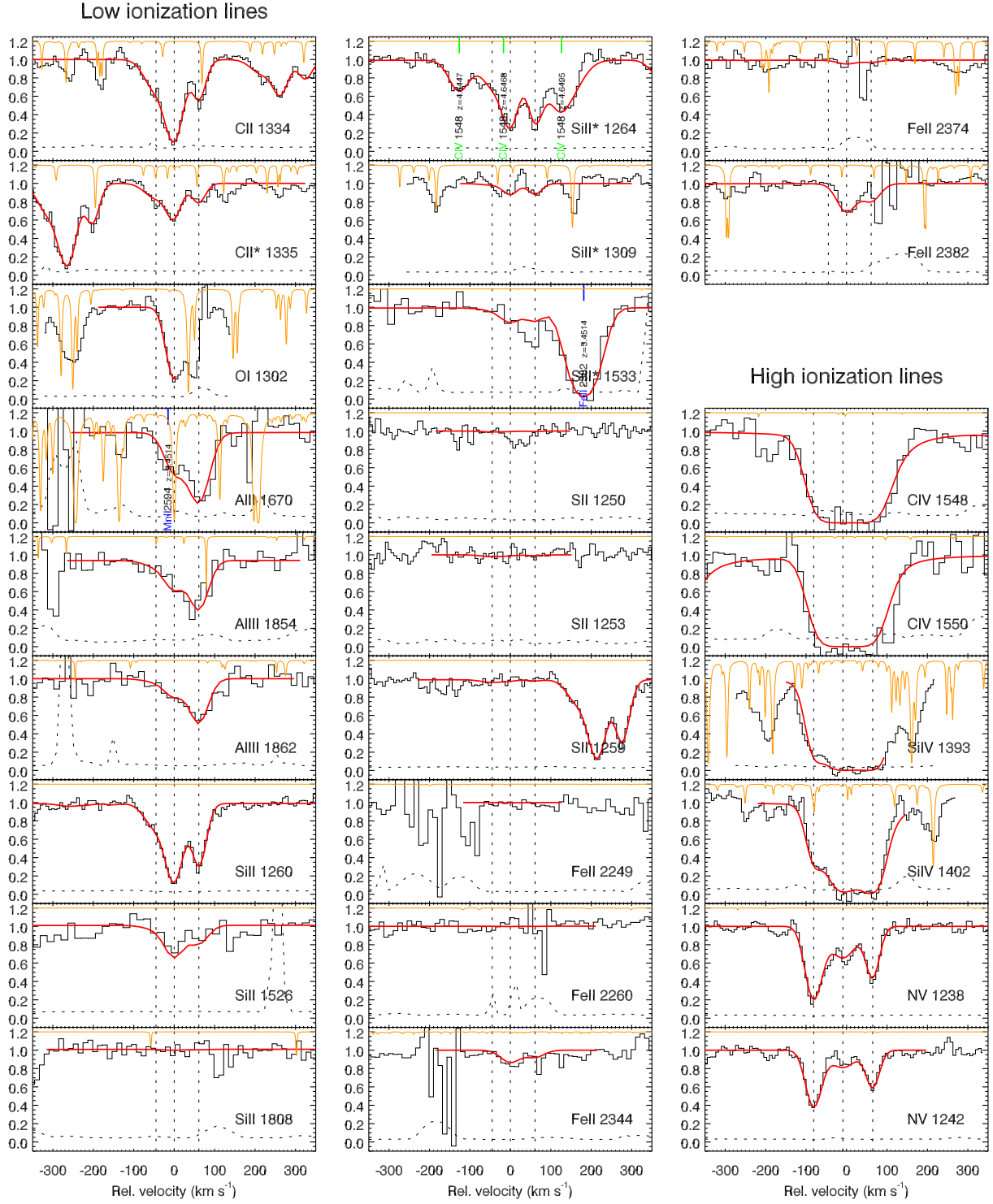


Fig. 5. Voigt-profile fits to the host-galaxy metal lines. We label the intervening metal lines (see Section 3.5) that contaminate the host galaxy lines; their contribution to the observed profile is taken into account. In orange we show a high-resolution atmospheric transmission spectrum for the observing site for an airmass of 1.50, slightly lower than that of our observations (see Table 1). Residuals such as those close to the Fe II lines are due to subtracted telluric emission lines.

it features a break at a redshift $z \sim 2.6$ after which it has a steep evolution (see Figure 6). Neeleman et al. (2013) reported a slightly flatter slope but found no evidence for a break. Using the definition by Prochaska & Wolfe (1997), ΔV is the width in velocity space containing 90% of the total optical depth of a line. For GRB 130606A we measure $\Delta V = 120 \pm 1 \text{ km s}^{-1}$ from the Si II $\lambda 1526$ transition, which is the best line available

for this analysis according to the criteria set by Ledoux et al. (2006). For a wider selection of lines (loosening these criteria) we find on average $\Delta V = 140 \pm 25 \text{ km s}^{-1}$, which is in agreement with the value of Si II $\lambda 1526$. GRB 130606A is the highest redshift object for which ΔV is determined and it is therefore well suited to address whether there is a break in the evolution of the MZ relation or not. We have included GRB 130606A into

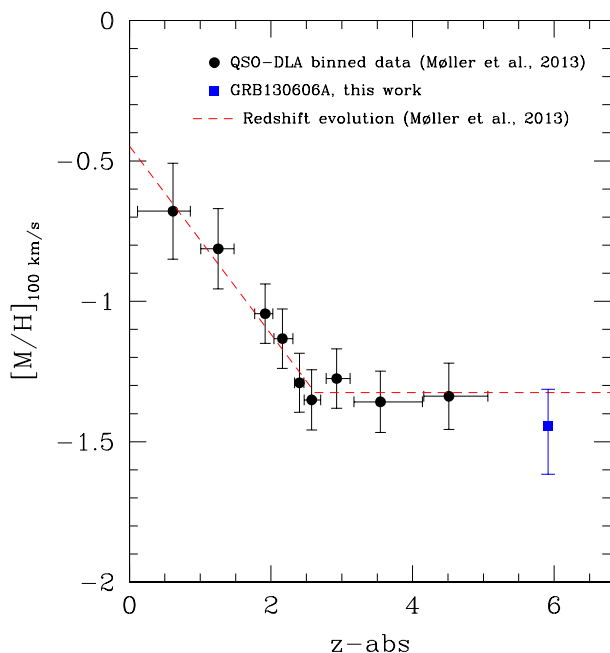


Fig. 6. Results from Møller et al. (2013) with included the high-redshift measurement of GRB 130606A. $[M/H]_{100 \text{ km/s}}$ is the metallicity expected for DLAs with $\Delta V = 100 \text{ km s}^{-1}$, based on the overall mass-metallicity relation. The data of Møller et al. (2013) (black filled circles) favour a break in the evolution of the mass-metallicity relation at $z \sim 2.6$ (dashed red line), which is also supported by our measurement of GRB 130606A (blue square). Assumed for this point are $\Delta V = 120 \text{ km s}^{-1}$ and $[M/H] = -1.33^{+0.13}_{-0.17}$; see text.

Figure 6 and keeping in mind that this is only a single point of a relation which has a significant internal scatter (0.38 dex in $[M/H]$), it is clearly seen that it is consistent the evolution with a break as reported in Møller et al. (2013). The metallicity adopted here is $[M/H] = -1.33^{+0.13}_{-0.17}$, which will be discussed in Section 4.2. The Neeleman et al. (2013) relation (less steep and with no break) predicts a much lower metallicity for this ΔV : $[M/H] = -2.25 \pm 0.75$. This value is marginally in agreement with our metallicity measurement thanks to the large scatter.

3.4.2. Fine-structure and metastable lines

Absorption lines from $\text{Si II } ^2P_{3/2}^{\circ}$ (Si II^*), that were first detected in a high- z GRB spectrum by Kawai et al. (2006), are also detected in GRB 130606A, and indicate that a considerable fraction of these ions are in an excited state (32% of total Si II; see Table 3). However, fine-structure and metastable lines from Fe II and Ni II, which are also usually present in high S/N GRB afterglow spectra (see e.g., Vreeswijk et al. 2007; Hartoog et al. 2013), are not convincingly detected here. By assuming that these lines have the same velocity structure (i.e. keeping z and b fixed) as the resonance lines, we have estimated upper limits on the gas-phase column densities of $\text{Fe II } ^6D_{7/2}$ (Fe II^*) and $\text{Ni II } ^4D_{9/2}$ (Ni II^*), which are listed in Table 3. A likely explanation of why these lines are absent is that the host of GRB 130606A is a relatively weak absorber for a GRB host (not even a DLA), and that the populations of the ground state level of these excited ions are already very low due to the combined effect of a low gas column and dust depletion (Section 3.4.4).

3.4.3. Ionisation correction

Because the neutral hydrogen column density is relatively low (sub-DLA), the hydrogen and the metals in the interstellar medium (ISM) are less shielded from ionising photons than in a DLA. As a result, the assumption that the overwhelming majority of an element is in a single neutral or lowly ionised state (e.g., $N_{\text{Si II}}/N_{\text{H I}} = N_{\text{Si}}/N_{\text{H}}$), which is valid for DLAs (Vladilo et al. 2001; Prochaska et al. 2002), might not hold for this system. It has been shown that the ionisation corrections for sub-DLAs are still small ($\lesssim 0.2$ dex, Dessauges-Zavadsky et al. 2003) barring a few strange cases (e.g., Milutinovic et al. 2010). For a GRB host galaxy, the situation prior to the GRB does not have to be similar to the situation in a QSO-sub-DLA, since the GRB host is actively forming stars and the gas is affected by the UV-radiation from the young stellar population, while this does not necessarily happens in a line-of-sight object. However, due to lack of information, we will assume that the ionisation corrections in the pre-GRB host situation are similar to those in QSO-sub-DLAs. Another aspect is the ionisation effect due to the rest-frame UV afterglow of the GRB. Both effects are investigated in this section.

For an estimate of the pre-burst ionisation correction we compare the situation with sub-DLA ionisation studies from the literature. Dessauges-Zavadsky et al. (2003) report on a detailed study with a sample of QSO-sub-DLAs, and use the logarithmic ratio $[\text{Al II}/\text{Al III}]$ or $[\text{Fe II}/\text{Fe III}]$ as an indicator for the degree of ionisation to calibrate the ionisation parameter U in their photoionisation model. For GRB 130606A, we measure $[\text{Al II}/\text{Al III}] = 0.81 \pm 0.80$ which is a typical value for sub-DLAs. The line profiles of the Al II and Al III lines are very similar to each other, which is an indication that the two different ionisation stages are located in the same physical regions in the galaxy (Dessauges-Zavadsky et al. 2003). The conclusion of this work is that sub-DLAs need small corrections $\lesssim 0.2$ dex for all measured elements except Al and Zn, that are more strongly influenced. The sub-DLA in GRB 130606A is very similar to the $z = 3.142$ sub-DLA in QSO PSS J2155+1258, presented in Figure 32 in Dessauges-Zavadsky et al. (2003). From this analogy we estimate that $\log U \sim -2.3$ for the pre-burst ionisation in the sub-DLA in GRB 130606A. Assuming this U and our measured $\log N_{\text{H I}} = 19.94$, the models by Meiring et al. (2009) give corrections $\epsilon_{\text{Si}} \sim -0.30$ and $\epsilon_{\text{Fe}} \sim -0.05$, with $\epsilon_{\text{X}} = [\text{X}/\text{H}]_{\text{total}} - \text{X}^+/\text{H}^0$. Vladilo et al. (2001) present a similar study with DLAs, but since our sub-DLA has a column density close to the DLA lower limit, we can extrapolate their model results down to $\log N_{\text{H I}} \sim 20$ yielding $\epsilon_{\text{Si}} \sim -0.21$, $\epsilon_{\text{S}} \sim -0.30$, $\epsilon_{\text{Fe}} \sim -0.04$ and $\epsilon_{\text{Ni}} \sim -0.17$. Note that these corrections are negative ($\text{X}^+/\text{H}^0 > [\text{X}/\text{H}]_{\text{total}}$), meaning that parts of singly ionised metals are in regions where hydrogen is ionised instead of neutral, because the lower column density shields itself less effectively.

The ionisation due to the afterglow of GRB 130606A is calculated in a method similar to what is used in De Cia et al. (2012) and Vreeswijk et al. (2013). From published near-IR photometry of GRB 130606A (Nagayama 2013b; Butler et al. 2013; Im et al. 2013; Morgan 2013; Afonso et al. 2013), and assuming a constant spectral index $\beta = -1$ (see Section 3.2) and a single power-law light curve, we obtain a temporal index $\alpha = -1$, at least until the time the spectrum is taken. The absorbing cloud is at distance d from the GRB, and is illuminated on one side by the afterglow between t_0 and t_{obs} , the time of our observations. The onset of the afterglow t_0 is

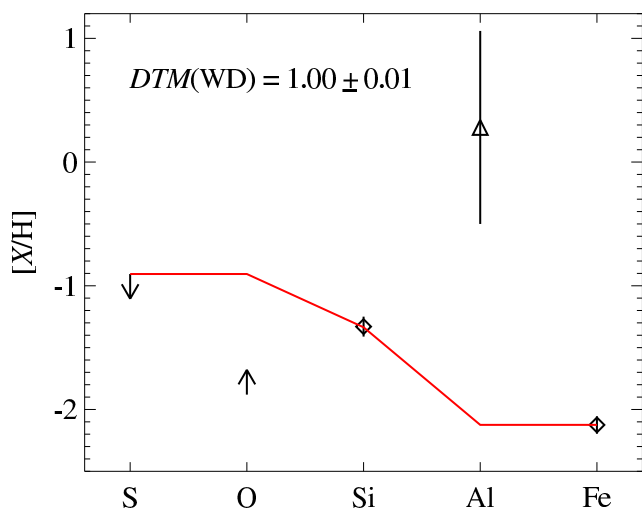


Fig. 7. Galactic warm disk depletion abundance pattern (solid line, [Savage & Sembach 1996](#)), in which Al is assumed to be depleted as strongly as Fe ([Phillips et al. 1982](#)), and depletion of O is assumed to be negligible ([Jenkins 2009](#)), fit to the observed pattern (diamonds) following [Savaglio \(2001\)](#). This fit ($\chi^2/\text{dof} = 0.002$) yields $\text{DTM} = 1.00 \pm 0.01$. Aluminum is not included in this fit. The limit on S is taken from [Castro-Tirado et al. \(2013a\)](#).

unknown and introduces an uncertainty; we assume different values to see its effect. The free parameters are the pre-burst $N_{\text{H I}}$ and $N_{\text{Fe II}}$. The distance d is obtained from a separate fit using the observed ratio $N_{\text{Si II}^*}/N_{\text{Si II}}$ in the cloud, and is estimated to be $d = 2.1 \pm 0.5$, 1.9 ± 0.4 and 1.8 ± 0.4 kpc for respectively $t_0 = 60$, 180 and 300 s in the rest frame. These values are in reasonable agreement with the lower limit $d > 2.2 \pm 0.2$ kpc derived from the upper limit of $N_{\text{Fe II}^*}/N_{\text{Fe II}}$. The column densities of the ions (except H I and Fe II), are put in at the start of the simulation with their measured values (Table 3). This is not fully correct, but it shows how much they would change when placed at the distance d , and be illuminated by the afterglow. From the differences in column density between t_0 and t_{obs} we conclude that the ionisation effects due to the afterglow are very minor. H I did not change at all, Fe II is lowered by 0.03 dex, O I by 0.01, Si II by 0.02, C II by 0.01, Al II by 0.02 and Al III by 0.01 dex by using $t_0 = 60$ s and even lower for the higher values of t_0 and the larger distance $d > 2.2$ kpc. $[\text{Al II}/\text{Al III}]$ is in all scenarios changed by < 0.01 dex, so this ratio can indeed be used to estimate the pre-burst conditions.

The two ionisation corrections work in opposite directions: the pre-burst ionisation has a stronger effect on the H I column density, while the GRB afterglow only has a small effect on the metals. We ignore here that the pre-burst situation did not have the ~ 2 kpc stretch of fully ionised and/or swept-up material due to the GRB. Because our estimates for the ionisation corrections are not the result of fully consistent modeling, we do not apply them directly to our measured abundances. We discuss in Section 4.2 the estimated metallicity when the corrections are taken into account.

3.4.4. Dust depletion

Although the optical extinction in the line of sight is low ($A_V < 0.2$ mag at the 3σ level, see Section 3.2), the abundance pattern (Table 3) suggests that there is dust depletion at play. Elements that are locked up into dust by greater amounts (e.g. Si, Fe) have

lower column densities in the gas phase than non-depleted elements (e.g. S), when compared to the relative abundance pattern in the solar photosphere ([Savage & Sembach 1996](#); [Phillips et al. 1982](#); [Jenkins 2009](#)).

For the analysis of the dust depletion we assume that the metallicity is $[\text{S}/\text{H}] = -0.91$ (using the limit $\log N_{\text{S}} < 14.17$ from [Castro-Tirado et al. 2013a](#)) and we include only Si and Fe in the depletion-pattern fit. We follow the method described by [Savaglio \(2001\)](#) and refer to depletion levels reported by [Savage & Sembach \(1996\)](#). We assume the depletion of oxygen to be negligible ([Jenkins 2009](#)) and the depletion of aluminum to be the same as iron, as suggested in [Phillips et al. \(1982\)](#). The observed abundances are formally best fit by the depletion pattern typical of a warm disk (WD) environment ($\chi^2/\text{dof} = 0.002$), although the other Galactic depletion patterns ([Savage & Sembach 1996](#)) can not be ruled out based on these two measurements. The results are displayed in Figure 7. Aluminum is a clear outlier. We exclude it from the fit because its abundance ($\log N_{\text{Al II}} = 14.66 \pm 0.78$) is clearly peculiar and therefore we cannot assume that the intrinsic relative abundance is similar to solar, which is pertinent to the depletion pattern analysis. There must be some process that causes an Al enhancement which we will discuss in Section 4.3.1.

The dust-to-metals ratio (DTM, expressed as a fraction of the average Local Group value, [Watson 2011](#)) derived from the depletion-pattern analysis ($\text{DTM} = 1.00 \pm 0.01$) agrees well with the one derived based only on the observed $[\text{Si}/\text{Fe}]$ ($\text{DTM} = 1.03 \pm 0.04$), using the method described in [De Cia et al. \(2013\)](#). A similar DTM is also found when other depletion patterns are used. Thus, assuming the underlying pattern is similar to that of a solar environment (see Section 4.3), the dust-to-metals ratio of the host galaxy environment is consistent with the Local Group value, which is remarkable at this redshift.

3.5. Intervening absorption systems

We confirm the detection of several intervening absorbers beside the host galaxy. Based on the preliminary reduction of the same X-shooter spectrum as discussed here, [Xu et al. \(2013a\)](#) reported $z_1 = 2.3103$ (Mg II) and $z_3 = 3.4515$ (Mg II, Fe II), which we confirm. We further detect $z_2 = 2.5207$ (Mg II, Fe II), $z_4 = 4.6448, 4.6468, 4.6495$ (C IV, Mg II, Al II, Si II, Fe II) reported earlier by [Chornock et al. \(2013\)](#). We can not unambiguously confirm the existence of the $z_5 = 5.806$ system reported by these authors. Lines that are possibly present are O I $\lambda 1302$, S II $\lambda 1260, \lambda 1265$, but many strong features are lacking: we do not see any Fe II transitions, no Si II $\lambda 1526$, no C IV $\lambda 1548$, although the expected locations of these intrinsically strong lines are in regions with high S/N and only little telluric contamination, and should not be blended with the other identified absorbers. We also report on a number of possible additional C IV absorbers which are less secure because only a single line or doublet can be associated with these systems: $z = 4.4660, 4.5309, 4.5427, 4.6497, 4.7244$.

3.6. Ly α forest constraints on the IGM

In this section we analyse the ionisation state of the IGM at $z \sim 5 - 6$ via the Gunn-Peterson optical depth ([Gunn & Peterson 1965](#)).

Table 3. Derived column densities from the host-galaxy absorption lines. The redshift and b parameters of the components for low and high ionisation species are listed in Table 2. Column densities are given as $\log(N/\text{cm}^{-2})$.

Low ionisation or neutral species					
Ion	$\log N_2$	$\log N_4$	$\log N_5$	$\log N_{\text{tot}}$	[X/H]
C II	13.79 ± 0.14	$> 15.00^a$	13.83 ± 0.10	> 15.04	[C/H] $> -1.29^b$
C II*	13.40 ± 0.15	13.70 ± 0.09	13.38 ± 0.11	14.01 ± 0.06	
O I	–	14.87 ± 0.12	–	> 14.75	[O/H] $> -1.88^c$
Al II	–	12.72 ± 0.22	14.63 ± 0.83	14.66 ± 0.78	[Al/H] = $+0.28 \pm 0.78^d$
Al III	12.28 ± 0.54	12.98 ± 0.14	13.75 ± 0.23	13.85 ± 0.19	
Si II	12.73 ± 0.13	13.73 ± 0.15	13.42 ± 0.18	13.95 ± 0.11	[Si/H] = -1.33 ± 0.08^b
Si II*	12.55 ± 0.16	13.28 ± 0.07	13.26 ± 0.11	13.62 ± 0.06	
S II	13.55 ± 0.31	12.95 ± 1.04	13.02 ± 0.74	$< 14.44^e$	[S/H] < -0.63
Fe II	–	13.09 ± 0.05	12.82 ± 0.17	13.29 ± 0.07	[Fe/H] = -2.12 ± 0.08
Fe II*	< 11.80	< 11.80	< 11.80	< 12.10	
Ni II	–	< 13.83	< 13.91	< 14.22	[Ni/H] $< +0.13^b$
Ni II*	< 12.92	< 12.90	< 13.14	< 13.45	
High ionisation species					
Ion	$\log N_1$	$\log N_3$	$\log N_6$	$\log N_{\text{tot}}$	
N V	13.79 ± 0.06	14.04 ± 0.09	14.33 ± 0.04	14.59 ± 0.03	

Notes. ^aThis component is likely saturated; we obtain a minimum $\log N$ from the equivalent width of the component.

^bBased on sum of ground state and excited state.

^cLower limit because both component 5 and the excited state column density cannot be measured due to telluric contamination.

^dBased on only Al II. The sum of Al II and Al III results in [Al/H] = $+0.43 \pm 0.62$.

^e 1σ upper limit because the relative strength of the components does not resemble the clearly detected lines, and therefore, we are measuring the noise.

Table 2. Redshift and Doppler parameter of the velocity components fitted to the metal lines of low and high ionisation species and for the fit to the Ly α line. v_{rel} is the velocity relative to that of component 4 (arbitrary).

Component	z	v_{rel} (km s ⁻¹)	b (km s ⁻¹)
Ly α	5.91248 ± 0.00028	-16	74 ± 7
components of low-ionisation lines			
2	5.91182 ± 0.00002	-45	14 ± 2
4	5.91285 ± 0.00002	0	10 ± 2
5	5.91426 ± 0.00020	+61	31 ± 10
components of high-ionisation lines			
1	5.91098 ± 0.00009	-81	37 ± 9
3	5.91265 ± 0.00003	-9	16 ± 2
6	5.91434 ± 0.00020	+64	31 ± 10

3.6.1. Ly α absorption

We measure Ly α absorption by the IGM from 1200 Å in the rest frame, which is the limit not affected by the blue wing of Ly α , to 1040 Å, the shortest wavelength that is not affected by possible Ly β emission from the GRB host. Within this range, we used redshift intervals of Δz of 0.15, which corresponds to ~ 60 Mpc in comoving distance, for comparison purposes with previous work. Using this redshift range and wavelength interval, we measure the transmission as

$$\mathcal{T}(z_{\text{abs}}) \equiv \langle f_{\nu}^{\text{obs}} / f_{\nu}^{\text{int}} \rangle. \quad (1)$$

The measured transmitted flux (\mathcal{T}) is shown in Table 4 and plotted in Figure 8. The continuum level is determined first by fitting a power law to the near-infrared part of the spectrum, taking advantage of the large wavelength coverage of X-shooter. Then, we fixed the slope, and fit the normalisation to the optical part of the spectrum (8530 – 8950 Å). We masked strong identified absorption features (both telluric and extragalactic) in this process.

When using QSOs for this kind of analysis, continuum determination is often the largest source of uncertainty, due to the complicated shape of their spectrum. A GRB continuum can be more accurately predicted due to its relatively flat shape without broad features. We estimate errors on the transmission by changing the continuum slope within 1σ (see Section 3.2), added in quadrature to the noise in the spectra and the errors in determining the unabsorbed continuum level. The latter dominates the errors on \mathcal{T} .

It is conventional to express optical depth τ in terms of $\tau = -\ln(\mathcal{T})$. We present τ as a function of redshift in Figure 9.

3.6.2. Ly β absorption

At the same neutral hydrogen density, the optical depth τ is proportional to $f\lambda_0$, where f and λ_0 are the oscillator strength and rest-frame wavelength of the transition, respectively. Therefore, the optical depth of Ly β is a factor of 6.2 smaller than that of Ly α , in a homogeneous medium illuminated by a uniform radiation field. Thus, Ly β probes into a larger amount of neutral hydrogen than Ly α . In this section we measure optical depth using Ly β absorption from the spectra.

We assume the same continuum as was used for Ly α . We choose the minimum wavelength to be 970 Å, above which it is not affected by Ly γ absorption. This results in a redshift range of $5.59 < z_{\text{abs}} < 5.74$ for Ly β . The Ly β absorptions overlap with Ly α absorption at lower redshift. Therefore, the Ly α absorption has to be corrected in measuring τ_{β} . We use Fan et al. (2006, their Equation 5) to estimate Ly α absorption from lower redshift, and corrected the Ly β transmission measurements. Table 4 shows the results, which are graphically represented in Figure 8 as blue diamonds.

To convert Ly β transmission to τ_{α} , one has to consider different optical depths between Ly α and Ly β . The difference depends on the UV background and its uniformity, the clumpiness of the

Table 4. IGM absorption towards the GRB 130606A at $z = 5.913$. The widths of bins are $\Delta z = 0.15, 0.15,$ and 0.06 for $\text{Ly}\alpha$, $\text{Ly}\beta$, and $\text{Ly}\gamma$ absorptions, respectively.

Redshift	Line	Transmission	τ_α
5.77	$\text{Ly}\alpha$	0.0052 ± 0.001	5.26 ± 0.14
5.62	$\text{Ly}\alpha$	0.0253 ± 0.001	3.68 ± 0.05
5.47	$\text{Ly}\alpha$	0.0767 ± 0.002	2.57 ± 0.02
5.33	$\text{Ly}\alpha$	0.1258 ± 0.004	2.07 ± 0.03
5.18	$\text{Ly}\alpha$	0.0868 ± 0.002	2.44 ± 0.03
5.02	$\text{Ly}\alpha$	0.0704 ± 0.002	2.65 ± 0.03
5.78	$\text{Ly}\beta$	0.051 ± 0.005	6.68 ± 0.09
5.62	$\text{Ly}\beta$	0.180 ± 0.006	3.86 ± 0.03
5.84	$\text{Ly}\gamma$	0.32 ± 0.024	5.0 ± 0.1
5.79	$\text{Ly}\gamma$	0.08 ± 0.016	18.2 ± 0.2

IGM, and its equation of state. According to simulations (e.g., Oh & Furlanetto 2005) and empirical measurements (Fan et al. 2006), the τ_α/τ_β conversion is in the range of 2.5–2.9. The τ_α/τ_γ conversion lies in the range of 4.4–5.7. Following the discussion in Fan et al. (2006), we use $\tau_\alpha/\tau_\beta = 2.25$ and $\tau_\alpha/\tau_\gamma = 4.4$.

Figure 9 shows constraints on the τ_α from $\text{Ly}\beta$ absorption measurements. Note that τ is converted to $\text{Ly}\alpha$ optical depth in Figure 9.

3.6.3. $\text{Ly}\gamma$ absorption

Similar to $\text{Ly}\beta$, the $\text{Ly}\gamma$ optical depth ($f\lambda_0$) is a factor of 17.9 smaller than that of $\text{Ly}\alpha$, providing us with a chance to probe into even more neutral hydrogen. The more neutral regions are denser in general. Therefore, $\text{Ly}\gamma$ transmission also provides the opportunity to probe regions with different density, potentially constraining the density-temperature relation.

The $\text{Ly}\gamma$ absorption measurement is restricted by the presence of $\text{Ly}\delta$ absorption at lower redshifts and the $\text{Ly}\gamma$ emission at the higher redshifts (closer to the GRB). Therefore, we use a smaller bin size of $\Delta z = 0.06$ than for the $\text{Ly}\alpha$ and $\text{Ly}\beta$ transmission. The $\text{Ly}\gamma$ transmission measurements are corrected for overlapping lower redshift $\text{Ly}\alpha$ and $\text{Ly}\beta$ absorptions using the best-fit power laws to lower redshift data (Fan et al. 2006, their Equations 5 and 6). The optical depth is converted to τ_α , using $\tau_\alpha/\tau_\gamma = 4.4$. The results are listed in Table 4 and shown in Figure 9.

The $\text{Ly}\gamma$ absorption measurements are much more challenging than those of $\text{Ly}\alpha$ and $\text{Ly}\beta$. Since the overlapping foreground $\text{Ly}\alpha$ and $\text{Ly}\beta$ lines absorb $\sim 98\%$ of the continuum flux in the wavelength ranges of $\text{Ly}\gamma$, we need to measure absorption in the remaining $\sim 2\%$. Errors in the continuum determination are also larger in this region since we use the bluer part of the spectrum.

In Figures 8 and 9, small triangles and gray squares represent previous data based on quasars from Fan et al. (2006) and Songaila (2004). The solid line shows the best power-law fit to the data at $z < 5.5$ based on Fan et al. (2006, their Equation 5). Within the scatter, our measurements are in agreement with earlier findings. At $z > 5.7$, our data points deviate from the fit to $z < 5.5$ data, suggesting that the Universe was not yet completely ionised at $z > 5.7$.

4. Discussion

4.1. Analysis of the red damping wing

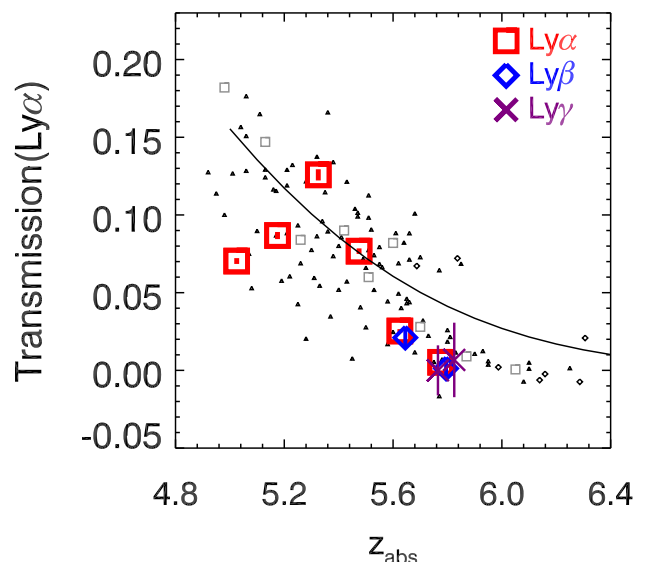


Fig. 8. $\text{Ly}\alpha$ transmission in the spectrum of GRB 130606A (red squares). $\text{Ly}\beta$ (blue diamonds) and $\text{Ly}\gamma$ (purple crosses) measurements are converted to equivalent values at $\text{Ly}\alpha$. The black triangles, diamonds, the gray squares are measurements based on quasars from Fan et al. (2006), Goto et al. (2011), and Songaila (2004), respectively. The solid line is the best power-law fit to the data at $z < 5.5$ by Fan et al. (2006, their Equation 5). The uncertainties of the QSO points are typically a factor two.

Totani et al. (2014) report evidence for a high neutral fraction based on their spectrum of the afterglow. In particular they find that a Voigt-profile fit to the red wing of the absorption trough is inconsistent with the data in a region referred to as wavelength range III by these authors, from about 8650 to 8700 Å. In Figure 10 we show wavelength range III in our spectrum including our fit and the deviations from the fit. Our spectrum is fully consistent with the Voigt-profile fit without a neutral hydrogen IGM component (see also Section 3.3). One important difference between our analysis and that of Totani et al. (2014) is that the value of the spectral slope adopted by latter ($\beta = -0.74$) is inconsistent with the one we find. Given that our spectral slope is derived from a much wider spectral range extending out to the K -band we think that the value of β adopted by Totani et al. (2014) is too low.

4.2. Metallicity of the host of GRB 130606A

The ‘raw’ measured column density values and limits we derive for the host-galaxy ISM (Table 3) are in good agreement with the results from Chornock et al. (2013) and Castro-Tirado et al. (2013a). Because our data have a higher spectral resolution and a larger wavelength coverage, we try to explain the effects of ionisation and dust depletion in order to better constrain metallicity and true abundance pattern in the host galaxy of GRB 130606A. Estimates on the effects of ionization are estimated in Section 3.4.3. Here, we discuss their possible implications. We will assume the pre-burst ionisation corrections for DLAs by Vladilo et al. (2001), which we extrapolate to our $\log N_{\text{H I}} = 19.94 \pm 0.01$. We measure $[\text{S}/\text{H}] < -0.62$ to which we apply a pre-burst correction of -0.30 dex. The ionisation correction of S due to the burst is not calculated but expected to be of order $+0.02$ dex. This results in $[\text{S}/\text{H}]_{\text{ic}} < -0.90$. Sulphur does not deplete onto dust, so this should reflect a real upper limit on the metallicity. The spectrum by Castro-Tirado et al. (2013a) is

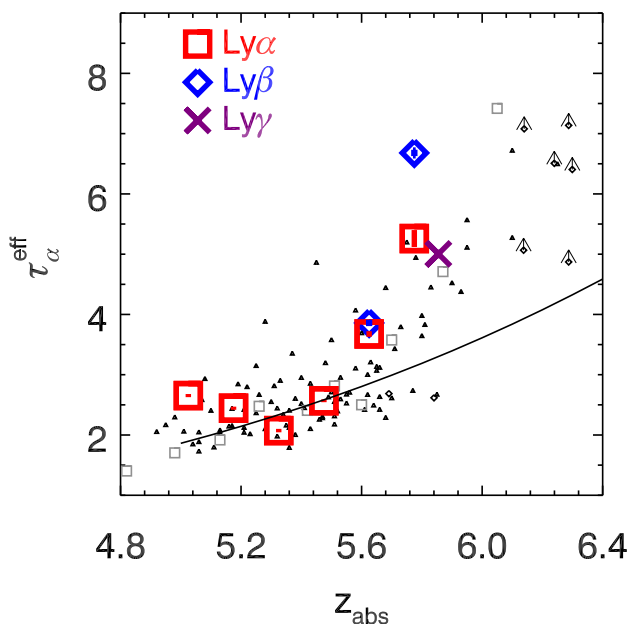


Fig. 9. Effective Gunn-Peterson $\text{Ly}\alpha$ optical depth of the IGM from the spectrum of GRB 130606A. The red squares, blue diamonds, and purple crosses are measurements with error estimates from $\text{Ly}\alpha$, $\text{Ly}\beta$ and $\text{Ly}\gamma$, respectively, the latter two converted to $\text{Ly}\alpha$ optical depth. The black triangles, diamonds, and the gray squares are measurements based on QSO spectra from Fan et al. (2006), Goto et al. (2011), and Songaila (2004), respectively. The uncertainties of the QSO points are typically a factor two. The solid line is the best power-law fit to the data at $z < 5.5$ by Fan et al. (2006, their Equation 5).

taken earlier in time, so from their $\log N_S < 14.17$ we obtain a more stringent upper limit for $[\text{S}/\text{H}]$ of < -0.91 , which after the ionisation correction would be $[\text{S}/\text{H}]_{\text{ic}} < -1.19$. We measure $[\text{Si}/\text{H}] = -1.33 \pm 0.08$; the pre-burst ionisation correction

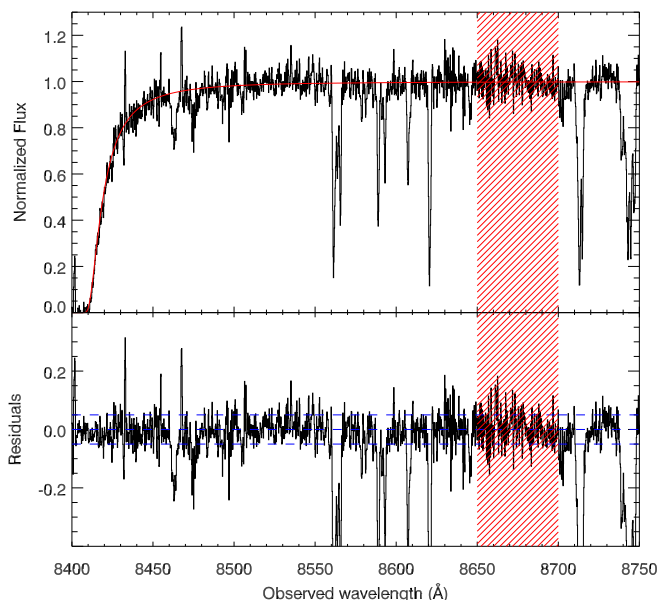


Fig. 10. Excerpt of the X-shooter spectrum with the same model fit as shown in Figure 3. The lower panel shows the residuals and the deviations from the fit. The red hatched region is range III in Totani et al. (2014), where their spectrum is inconsistent with a single DLA model. With our data, we can obtain a good fit with this model. The difference is likely due to a different spectral index β , see Section 4.1.

of -0.21 dex, and the GRB afterglow effect of $+0.02$ dex result in $[\text{Si}/\text{H}]_{\text{ic}} = -1.52$. The measured $[\text{Fe}/\text{H}] = -2.12 \pm 0.08$ is not severely affected by ionisation: the pre-burst correction is -0.04 dex and that of the afterglow is $+0.03$ dex, resulting in $[\text{Fe}/\text{H}]_{\text{ic}} = -2.11$. Assuming a solar abundance pattern, there is still evidence for dust depletion, but even without fitting the pattern, the metallicity should be $-1.5 < [\text{M}/\text{H}] < -1.2$, since Si provides a lower limit. This is relatively high when compared to QSO-DLAs at $z > 5$ (Rafelski et al. 2012, 2014). The difference in metallicity evolution in GRB-DLAs and QSO-DLAs is also discussed recently in e.g., Thöne et al. (2013); Sparre et al. (2014) and Cucchiara et al. (2014).

4.3. Nucleosynthetic history

The high value of $[\text{Si}/\text{Fe}]$ can be fully attributed to dust depletion, but the effects of this, and those of an underlying pattern that is different from that in the solar photosphere (e.g., α -element enhancement), are degenerate. At this redshift, one would expect to see more elements in the ISM created by shorter-lived massive stars, α -elements (C, N, O, Ne, Mg, S, Si, Ar, Ca, Ti) from core-collapse supernovae (SNe), rather than products of SNe originating in longer living stars: the iron peak elements created by Type Ia SNe (V, Cr, Mn, Fe, Co, Ni). This has not unambiguously been detected in high redshift GRB host galaxies to date, because there is usually the combined effect of the dust depletion (see e.g., Thöne et al. 2013; Sparre et al. 2014). With the limited information we have for GRB 130606A, we cannot draw strong conclusions on either the dust depletion or α -element enhancement. With a pure dust-depletion explanation, the dust-to metals ratio is about the same as the Local Group value. The dust extinction ($A_V < 0.2$ mag at 3σ) can still be low due to the low total metal column density (see also, e.g., Zafar et al. 2011). A peculiarity that we can not explain with dust depletion is the very high abundance of aluminum, which we discuss in Section 4.3.1.

4.3.1. High aluminum abundance in the host of GRB 130606A

The analysis of the X-shooter spectrum of the host galaxy of GRB 130606A yields a remarkably high aluminum abundance: $[\text{Al II}/\text{H I}] = +0.28 \pm 0.78$ (even $[(\text{Al II} + \text{Al III})/\text{H I}] = +0.43 \pm 0.62$), given the low iron abundance of $[\text{Fe}/\text{H}] = -2.12 \pm 0.08$. The dust depletion effect on these two elements is expected to be very similar (Phillips et al. 1982). A relatively high aluminum abundance has been measured in the atmospheres of red giants in metal-poor ($[\text{Fe}/\text{H}] < -1$) globular clusters (e.g., Kraft et al. 1997), although $[\text{Al}/\text{Fe}]$ seems to be always ≤ 1.5 (Cordero et al. 2014), while we find $+2.40 \pm 0.78$. In these globular clusters a strong anti-correlation has been found between the oxygen and sodium abundance. This anti-correlation has been interpreted as being due to proton-capture nucleosynthesis, where Na and Al are produced at the expense of Ne and Mg in regions where C and O are converted into N, i.e. where the CNO cycle is active (Cavallo et al. 1998). Regarding these metal-poor globular clusters, the question is: did the proton capture occur within the observed red giants, i.e. during shell burning when the temperature is high enough for the CNO cycle, and convection managed to dredge up the metals produced in these deeper layers within the stars (evolutionary scenario)? Or were these abundance “anomalies” produced by proton capture in a previous generation of massive (perhaps even the first) stars (primordial scenario)? The detection of similar abundance anomalies in main-sequence,

turn-off and early sub-giant stars (Gratton et al. 2001) suggests the latter scenario. Denissenkov & Hartwick (2014) propose that the abundance anomalies of proton-capture elements in globular clusters were produced by supermassive stars with $M \sim 10^4 M_{\odot}$, products of the runaway collisions of massive stars in dense clusters (Portegies Zwart et al. 2004).

In the host galaxy of GRB 130606A, the oxygen abundance is low: Chornock et al. (2013) find $[O/H] \sim -2.0$, and we derive a lower limit of $[O/H] > -1.88$. Unfortunately, the nitrogen, sodium and magnesium abundances could not be determined, although we see presence of nitrogen in particularly strong N v lines. In the host galaxy of GRB 120327A ($z = 2.8145$, D’Elia et al. 2014) also a high aluminum abundance is measured $[Al/H] = 0.00 \pm 0.11$; $[Al/Fe] = 1.73 \pm 0.07$, though saturation of the Al II and Al III lines prevents an accurate abundance analysis of the three individual absorption line components. The oxygen abundance is low ($[O/H] = -1.98 \pm 0.13$) with respect to iron ($[Fe/H] = -1.73 \pm 0.10$), the nitrogen abundance higher ($[N/H] = -1.45 \pm 0.11$), but the magnesium abundance is not very low ($[Mg/H] = -1.27 \pm 0.10$). However, in metal-poor globular clusters (e.g. M22, M4, 47 Tuc) Al is always enhanced, irrespective of Mg; only in M13 a strong Mg/Al anti-correlation has been observed (Kraft et al. 1997). In the host galaxy of GRB 120327A also the silicon abundance is high ($[Si/H] = -1.16 \pm 0.09$); Si would be produced by proton capture of Al. The Si abundance in the host galaxy of GRB 130606A is $[Si/H] = -1.33 \pm 0.08$, much higher than the Fe abundance ($[Fe/H] = -2.12 \pm 0.08$), although this can be completely due to dust depletion.

The measured abundances in these two GRB host galaxies seem to suggest that proton-capture has been at work. Given the high redshift ($z \sim 6$) of GRB 130606A, and the corresponding look-back time (~ 12.7 Gyr), these observations are consistent with the scenario that a previous generation of massive stars must have produced the chemical enrichment due to proton capture.

4.4. Reionisation of the IGM

Prompt follow-up spectroscopy of GRB 130606A has enabled to robustly measure of Gunn-Peterson optical depths using a GRB instead of a QSO as a background source (see also Chornock et al. 2013; Totani et al. 2014). The only other GRB for which this has been attempted is GRB 050904 (Totani et al. 2006). Given a high S/N afterglow spectrum, GRBs have several advantages over QSOs; the simple power-law continuum of a GRB spectrum is much easier to estimate than the complicated shape of a QSO spectrum, including a possibly broken power-law UV continuum, whose break is in the heavily absorbed UV range at high-redshift, and broad emission lines. As a consequence of this, the uncertainties of the measured optical depths based on our GRB spectrum are much smaller than typical uncertainties on values in previous work based on QSOs, which are about a factor 2. In addition, GRBs can be much brighter than QSOs if observed early enough. At the time of our reported spectroscopy, GRB 130606A had a near-IR brightness (Y, J, H) of around the 18th magnitude (Butler et al. 2013). This is much brighter than $z \sim 6$ QSOs used in previous work ($m_z \sim 20$ mag). While obtaining high S/N spectra of fainter QSOs with current 8 m-class telescopes becomes progressively more difficult at higher redshift with fainter QSOs, by using GRBs we can in principle extend the Gunn-Peterson test to much higher redshifts, without having to rely on future larger optical telescopes.

Another advantage of GRBs over QSOs is that the sightlines towards them suffer from different biases. GRB host galaxies differ from typical field galaxies (Fruchter et al. 2006; Savaglio et al. 2009; Wang & Dai 2014). At low redshift they are found to be low-mass, metal poor galaxies, which reside in ‘representative’ regions of the Universe. On the other hand, QSOs tend to be contained in massive haloes. The surroundings of QSOs could be overdense on scales of several tens of Mpc (for example see Overzier et al. 2009; Utsumi et al. 2010). In this case, the IGM in front of QSOs could be more ionised than a typical region of the Universe. Furthermore, the QSO background light has been present for a long time, which may have affected the degree of ionisation of the material in the sight line, in particular close to the source: the proximity effect. This is not the case for GRB afterglows.

However, despite our accurate measurements, the optical depths show significant variation across the redshift window we used ($5.0 < z < 5.8$). The variation is much larger than our measurement errors, and therefore, intrinsic. This suggests a large spatial variation in optical depths at this epoch of the Universe. Therefore, to fully understand the reionisation history of the Universe, it is important to expand the statistical sample. GRBs will likely play a prominent role in this.

5. Conclusions

In this paper we report the analysis of the $z = 5.913$ GRB 130606A afterglow spectrum obtained with VLT/X-shooter. The analysis can be divided in two main parts: the study of the abundance pattern in the host galaxy measured by the afterglow absorption lines, and the study of the ionised fraction of the IGM through the shape of the red wing of Ly α at z_{GRB} , and by the Gunn-Peterson optical depth in front of the GRB ($5.02 < z < 5.84$).

Although many host absorption lines are detected, only for H, Si, Fe and Al the abundances can be well constrained; for C, O, S and Ni we obtain limits. The high $[Si/Fe] = +0.79 \pm 0.13$ can be explained with dust depletion with a dust-to-metals ratio similar to the Local Group value or α -element enhancement. The abundance of aluminum is very high: $[Al/H] = +0.28 \pm 0.78$ and $[Al/Fe] = +2.40 \pm 0.78$ based on Al II alone, and even higher when taking into account Al III, which shows a similar line structure suggesting that the region where this resides is associated with where Al II is located. With $\log N_{H I} = 19.94 \pm 0.01$ the absorber is a sub-DLA and might not be as efficiently shielding the ions from ionisation as DLAs. We estimate the ionisation corrections both in the pre-burst sub-DLA and due to the UV radiation GRB afterglow. While the former results in corrections up to 0.3 dex, the latter is in this case negligible with corrections below 0.03 dex. The metallicity, taking into account these corrections and the more stringent upper limit on S by Castro-Tirado et al. (2013a), is estimated to be $-1.5 < [M/H] < -1.2$ (3%–6% of solar). The metallicity and low-ionisation line width measured at this high redshift is are consistent the break in the evolution of the mass-metallicity relation for DLAs proposed in Møller et al. (2013), but also marginally with a model that assumes a shallower slope and no break (Neeleman et al. 2013).

By fitting the red wing of the Ly α absorption line of the GRB host galaxy, we conclude that the IGM is predominantly neutral: the ionised fraction $x_{H I} = 0$ ($x_{H I} < 0.03$ at 3σ significance). We measure the effective Gunn-Peterson Ly α optical depth of the IGM at $5.02 < z < 5.84$. Our well-constrained data points are in agreement with earlier test with background QSOs, that show that the IGM was increasingly neutral at $z > 5.6$ but still

overwhelmingly ionized. However, the intrinsic scatter within the measurement is much larger than the errors on the individual data points, likely reflecting that the reionisation is a complicated process with a strong spatial variation. A larger statistical sample is required to understand the IGM state at the end of reionisation.

Acknowledgements. We thank Max Pettini, Darach Watson and Georges Meynet for helpful discussions. We thank Andrea Rossi for careful reading of the manuscript. O.E.H acknowledges the Dutch Research School for Astronomy (NOVA) for a PhD grant. D.M acknowledges the Instrument center for Danish Astrophysics (IDA) for funding. The research leading to these results has received funding from the European Research Council under the European Union's Seventh Framework Program (FP7/2007-2013)/ERC Grant agreement no. EGG5-278202 (J. P. U. F.). T. K acknowledges support by the European Commission under the Marie Curie Intra-European Fellowship Programme in FP7. The research of A.d.U.P. is supported by the Spanish project AYA2012-39362-C02-02 and by the European Commission under the Marie Curie Career Integration Grant programme (FP7-PEOPLE-2012-CIG 322307). The Dark Cosmology Centre is funded by the DNRF.

References

- Afonso, P., Kann, D. A., Nicuesa Guelbenzu, A., et al. 2013, GRB Coordinates Network, 14807
- Andersen, M. I., Hjorth, J., Pedersen, H., et al. 2000, A&A, 364, L54
- Asplund, M., Grevesse, N., Sauval, A. J., & Scott, P. 2009, ARA&A, 47, 481
- Barthelmy, S. D., Baumgartner, W. H., Cummings, J. R., et al. 2013, GRB Coordinates Network, 14819
- Berger, E., Chary, R., Cowie, L. L., et al. 2007, ApJ, 665, 102
- Butler, N., Watson, A. M., Kutlyrev, A., et al. 2013, GRB Coordinates Network, 14799
- Castro-Tirado, A. J., Sánchez-Ramírez, R., Ellison, S. L., et al. 2013a, ArXiv e-prints, 1312.5631
- Castro-Tirado, A. J., Sanchez-Ramirez, R., Gorosabel, J., et al. 2013b, GRB Coordinates Network, 14796
- Cavallo, R. M., Sweigart, A. V., & Bell, R. A. 1998, ApJ, 492, 575
- Chornock, R., Berger, E., Fox, D. B., et al. 2013, ApJ, 774, 26
- Ciardi, B. & Loeb, A. 2000, ApJ, 540, 687
- Cordero, M. J., Pilachowski, C. A., Johnson, C. I., et al. 2014, ApJ, 780, 94
- Cucchiara, A., Fumagalli, M., Rafelski, M., et al. 2014, ArXiv e-prints, 1408.3578
- De Cia, A., Ledoux, C., Fox, A. J., et al. 2012, A&A, 545, A64
- De Cia, A., Ledoux, C., Savaglio, S., Schady, P., & Vreeswijk, P. M. 2013, A&A, 560, A88
- D'Elia, V., Fynbo, J. P. U., Goldoni, P., et al. 2014, A&A
- Denissenkov, P. A. & Hartwick, F. D. A. 2014, MNRAS, 437, L21
- Dessauges-Zavadsky, M., Péroux, C., Kim, T.-S., D'Odorico, S., & McMahon, R. G. 2003, MNRAS, 345, 447
- Deutsch, E. W. 1999, AJ, 118, 1882
- Evans, P. A., Beardmore, A. P., Page, K. L., et al. 2009, MNRAS, 397, 1177
- Evans, P. A., Beardmore, A. P., Page, K. L., et al. 2007, A&A, 469, 379
- Fan, X., Strauss, M. A., Becker, R. H., et al. 2006, AJ, 132, 117
- Fox, A. J., Ledoux, C., Vreeswijk, P. M., Smette, A., & Jaunsen, A. O. 2008, A&A, 491, 189
- Fox, A. J., Petitjean, P., Ledoux, C., & Srianand, R. 2007, A&A, 465, 171
- Fruchter, A. S., Levan, A. J., Strolger, L., et al. 2006, Nature, 441, 463
- Fynbo, J. P. U., Prochaska, J. X., Sommer-Larsen, J., Dessauges-Zavadsky, M., & Møller, P. 2008, ApJ, 683, 321
- Gehrels, N., Chincarini, G., Giommi, P., et al. 2004, ApJ, 611, 1005
- Giavalisco, M. 2002, ARA&A, 40, 579
- Goldoni, P. 2011, Astronomische Nachrichten, 332, 227
- Goto, T., Utsumi, Y., Hattori, T., Miyazaki, S., & Yamauchi, C. 2011, MNRAS, 415, L1
- Gratton, R. G., Bonifacio, P., Bragaglia, A., et al. 2001, A&A, 369, 87
- Greiner, J., Krühler, T., Fynbo, J. P. U., et al. 2009, ApJ, 693, 1610
- Gunn, J. E. & Peterson, B. A. 1965, ApJ, 142, 1633
- Hartoog, O. E., Wiersema, K., Vreeswijk, P. M., et al. 2013, MNRAS, 430, 2739
- Im, M., Sung, H.-I., & Urata, Y. 2013, GRB Coordinates Network, 14800
- Jelinek, M., Gorosabel, J., Castro-Tirado, A. J., et al. 2013, GRB Coordinates Network, 14782, 1
- Jenkins, E. B. 2009, ApJ, 700, 1299
- Kawai, N., Kosugi, G., Aoki, K., et al. 2006, Nature, 440, 184
- Komatsu, E., Smith, K. M., Dunkley, J., et al. 2011, ApJS, 192, 18
- Kraft, R. P., Sneden, C., Smith, G. H., et al. 1997, AJ, 113, 279
- Krühler, T., Greiner, J., Schady, P., et al. 2011, A&A, 534, A108
- Lamb, D. Q. & Reichart, D. E. 2000, ApJ, 536, 1
- Ledoux, C., Petitjean, P., Fynbo, J. P. U., Møller, P., & Srianand, R. 2006, A&A, 457, 71
- Lodders, K., Palme, H., & Gail, H.-P. 2009, Landolt Börnstein, 44
- Lunnan, R., Drout, M., Chornock, R., & Berger, E. 2013, GRB Coordinates Network, 14798
- Meiring, J. D., Lauroesch, J. T., Kulkarni, V. P., et al. 2009, MNRAS, 397, 2037
- Milutinovic, N., Ellison, S. L., Prochaska, J. X., & Tumlinson, J. 2010, MNRAS, 408, 2071
- Miralda-Escudé, J. 1998, ApJ, 501, 15
- Møller, P., Fynbo, J. P. U., Ledoux, C., & Nilsson, K. K. 2013, MNRAS, 430, 2680
- Monet, D., A., B., Canzian, B., et al. 1998, U.S. Naval Observatory, Washington DC
- Morgan, A. N. 2013, GRB Coordinates Network, 14802
- Nagayama, T. 2013a, GRB Coordinates Network, 14794
- Nagayama, T. 2013b, GRB Coordinates Network, 14784
- Neeleman, M., Wolfe, A. M., Prochaska, J. X., & Rafelski, M. 2013, ApJ, 769, 54
- Oh, S. P. & Furlanetto, S. R. 2005, ApJ, 620, L9
- Ono, Y., Ouchi, M., Mobasher, B., et al. 2012, ApJ, 744, 83
- Osborne, J. P., Beardmore, A. P., Evans, P. A., & Goad, M. R. 2013, GRB Coordinates Network, 14811
- Overzier, R. A., Guo, Q., Kauffmann, G., et al. 2009, MNRAS, 394, 577
- Patel, M., Warren, S. J., Mortlock, D. J., & Fynbo, J. P. U. 2010, A&A, 512, L3
- Pei, Y. C. 1992, ApJ, 395, 130
- Pentericci, L., Vanzella, E., Fontana, A., et al. 2014, ArXiv e-prints
- Phillips, A. P., Gondhalekar, P. M., & Pettini, M. 1982, MNRAS, 200, 687
- Portegies Zwart, S. F., Baumgardt, H., Hut, P., Makino, J., & McMillan, S. L. W. 2004, Nature, 428, 724
- Price, P. A., Songaila, A., Cowie, L. L., et al. 2007, ApJ, 663, L57
- Prochaska, J. X., Chen, H.-W., Dessauges-Zavadsky, M., & Bloom, J. S. 2007a, ApJ, 666, 267
- Prochaska, J. X., Dessauges-Zavadsky, M., Ramirez-Ruiz, E., & Chen, H.-W. 2008, ApJ, 685, 344
- Prochaska, J. X., Henry, R. B. C., O'Meara, J. M., et al. 2002, PASP, 114, 933
- Prochaska, J. X. & Wolfe, A. M. 1997, ApJ, 487, 73
- Prochaska, J. X., Wolfe, A. M., Howk, J. C., et al. 2007b, ApJS, 171, 29
- Rafelski, M., Neeleman, M., Fumagalli, M., Wolfe, A. M., & Prochaska, J. X. 2014, ApJ, 782, L29
- Rafelski, M., Wolfe, A. M., Prochaska, J. X., Neeleman, M., & Mendez, A. J. 2012, ApJ, 755, 89
- Ruiz-Velasco, A. E., Swan, H., Troja, E., et al. 2007, ApJ, 669, 1
- Salvaterra, R., Della Valle, M., Campana, S., et al. 2009, Nature, 461, 1258
- Savage, B. D. & Sembach, K. R. 1996, ARA&A, 34, 279
- Savaglio, S. 2001, in IAU Symposium, Vol. 204, The Extragalactic Infrared Background and its Cosmological Implications, ed. M. Harwit & M. G. Hauser, 307
- Savaglio, S., Glazebrook, K., & Le Borgne, D. 2009, ApJ, 691, 182
- Schlafly, E. F. & Finkbeiner, D. P. 2011, ApJ, 737, 103
- Schlegel, D. J., Finkbeiner, D. P., & Davis, M. 1998, ApJ, 500, 525
- Songaila, A. 2004, AJ, 127, 2598
- Sparre, M., Hartoog, O. E., Krühler, T., et al. 2014, ApJ, 785, 150
- Stark, D. P., Ellis, R. S., Chiu, K., Ouchi, M., & Bunker, A. 2010, MNRAS, 408, 1628
- Steidel, C. C., Adelberger, K. L., Shapley, A. E., et al. 2003, ApJ, 592, 728
- Tanvir, N. R., Fox, D. B., Levan, A. J., et al. 2009, Nature, 461, 1254
- Tanvir, N. R., Levan, A. J., Fruchter, A. S., et al. 2012, ApJ, 754, 46
- Thöne, C. C., Fynbo, J. P. U., Goldoni, P., et al. 2013, MNRAS, 428, 3590
- Totani, T., Aoki, K., Hattori, T., et al. 2014, PASJ, 66, 63
- Totani, T., Kawai, N., Kosugi, G., et al. 2006, PASJ, 58, 485
- Ukwatta, T. N., Barthelmy, S. D., Gehrels, N., et al. 2013, GRB Coordinates Network, 14781
- Utsumi, Y., Goto, T., Kashikawa, N., et al. 2010, ApJ, 721, 1680
- Vacca, W. D., Cushing, M. C., & Rayner, J. T. 2003, PASP, 115, 389
- Vernet, J., Dekker, H., D'Odorico, S., et al. 2011, A&A, 536, A105
- Vladilo, G., Centurión, M., Bonifacio, P., & Howk, J. C. 2001, ApJ, 557, 1007
- Vreeswijk, P. M., Ledoux, C., Raassen, A. J. J., et al. 2013, A&A, 549, A22
- Vreeswijk, P. M., Ledoux, C., Smette, A., et al. 2007, A&A, 468, 83
- Wang, F. Y., Bromm, V., Greif, T. H., et al. 2012, ApJ, 760, 27
- Wang, F. Y. & Dai, Z. G. 2014, ApJS, 213, 15
- Watson, D. 2011, A&A, 533, A16
- Wijers, R. A. M. J., Bloom, J. S., Bagla, J. S., & Natarajan, P. 1998, MNRAS, 294, L13
- Wolfe, A. M., Gawiser, E., & Prochaska, J. X. 2005, ARA&A, 43, 861
- Xu, D., Malesani, D., Schulze, S., et al. 2013a, GRB Coordinates Network, 14816
- Xu, D., Malesani, D., Schulze, S., et al. 2013b, GRB Coordinates Network, 14783
- Xu, Z. & Wei, D. 2009, Science in China G: Physics and Astronomy, 52, 1428
- Zafar, T., Watson, D., Fynbo, J. P. U., et al. 2011, A&A, 532, A143

-
- ¹ Anton Pannekoek Institute for Astronomy, University of Amsterdam, Science Park 904, PO Box 94249, 1090 GE Amsterdam, The Netherlands, e-mail: O.E.Hartoog@uva.nl
 - ² Dark Cosmology Centre, Niels Bohr Institute, Copenhagen University, Juliane Maries Vej 30, 2100 Copenhagen O, Denmark
 - ³ Institute of Astronomy and Department of Physics, National Tsing Hua University, No. 101, Section 2, Kuang-Fu Road, Hsinchu 30013, Taiwan, R.O.C
 - ⁴ European Southern Observatory, Alonso de Córdova 3107, Vitacura, Casilla 19001, Santiago 19, Chile
 - ⁵ Department of Particle Physics and Astrophysics, Faculty of Physics, Weizmann Institute of Science, Rehovot 76100, Israel
 - ⁶ European Southern Observatory, Karl-Schwarzschildstrasse 2, 85748 Garching bei München, Germany
 - ⁷ INAF, Osservatorio Astronomico di Brera, Via E. Bianchi 46, I-23807 Merate, Italy
 - ⁸ INAF-Osservatorio Astronomico di Roma, Via Frascati 33, I-00040 Monteporzio Catone, Italy
 - ⁹ ASI-Science Data Center, Via Galileo Galilei, I-00044 Frascati, Italy
 - ¹⁰ Laboratoire GEPI, Observatoire de Paris, CNRS-UMR8111, Univ. Paris-Diderot 5 place Jules Janssen, 92195 Meudon France
 - ¹¹ APC, Astroparticule et Cosmologie, Université Paris Diderot, CNRS/IN2P3, CEA/Irfu, Observatoire de Paris, Sorbonne Paris Cité, 10, Rue Alice Domon et Léonie Duquet, 75205, Paris Cedex 13, France
 - ¹² Centre for Astrophysics and Cosmology, Science Institute, University of Iceland, Dunhagi 5, IS-107 Reykjavk, Iceland
 - ¹³ Department of Physics, University of Warwick, Coventry CV4 7AL, United Kingdom
 - ¹⁴ The Oskar Klein Centre, Department of Astronomy, AlbaNova, SE-106 91, Stockholm, Sweden
 - ¹⁵ University of Leicester, Department of Physics and Astronomy, University Road, Leicester LE1 7RH, United Kingdom
 - ¹⁶ Instituto de Astrofísica de Andalucía (IAA-CSIC), Glorieta de la Astronomía s/n, E-18008, Granada, Spain
 - ¹⁷ Tuorla Observatory, Department of Physics and Astronomy, University of Turku, FI-20014 Turku, Finland
 - ¹⁸ Finnish Centre for Astronomy with ESO, University of Turku, Väisäläntie 20, 21500, Piikkiö, Finland
 - ¹⁹ Department of Physics and Astronomy, Michigan State University, East Lansing, MI 48824, USA
 - ²⁰ Institute of Theoretical Astrophysics, University of Oslo, P.O. Box 1029, Blindern, NO-0315 Oslo, Norway
 - ²¹ Institut d’Astrophysique Spatiale, CNRS (UMR8617) Université Paris-Sud 11, Bâtiment 121, Orsay, France

Appendix A: Absorption spectra

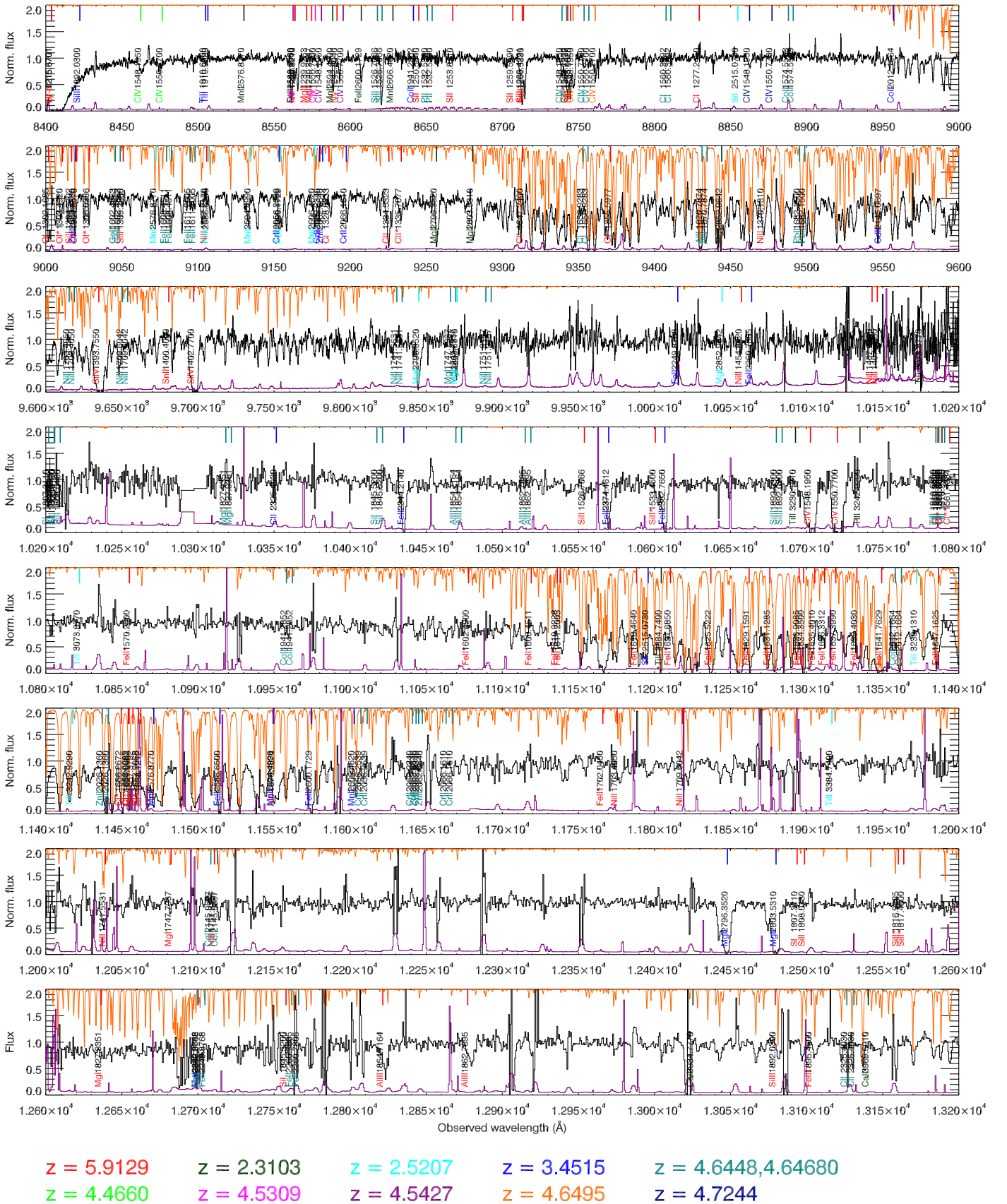


Fig. A.1. Afterglow spectrum of GRB 130606A, starting from Ly α . The absorption lines are indicated with the ion that produces them, and the rest wavelength. We use different colours for the various absorbers (see Section 3.5), as indicated in the legend; $z = 5.9127$ in red is the signature of the host galaxy. The error spectrum is shown in purple, the orange spectrum is the scaled atmospheric transmission spectrum. The spectrum continues in Figure A.2.

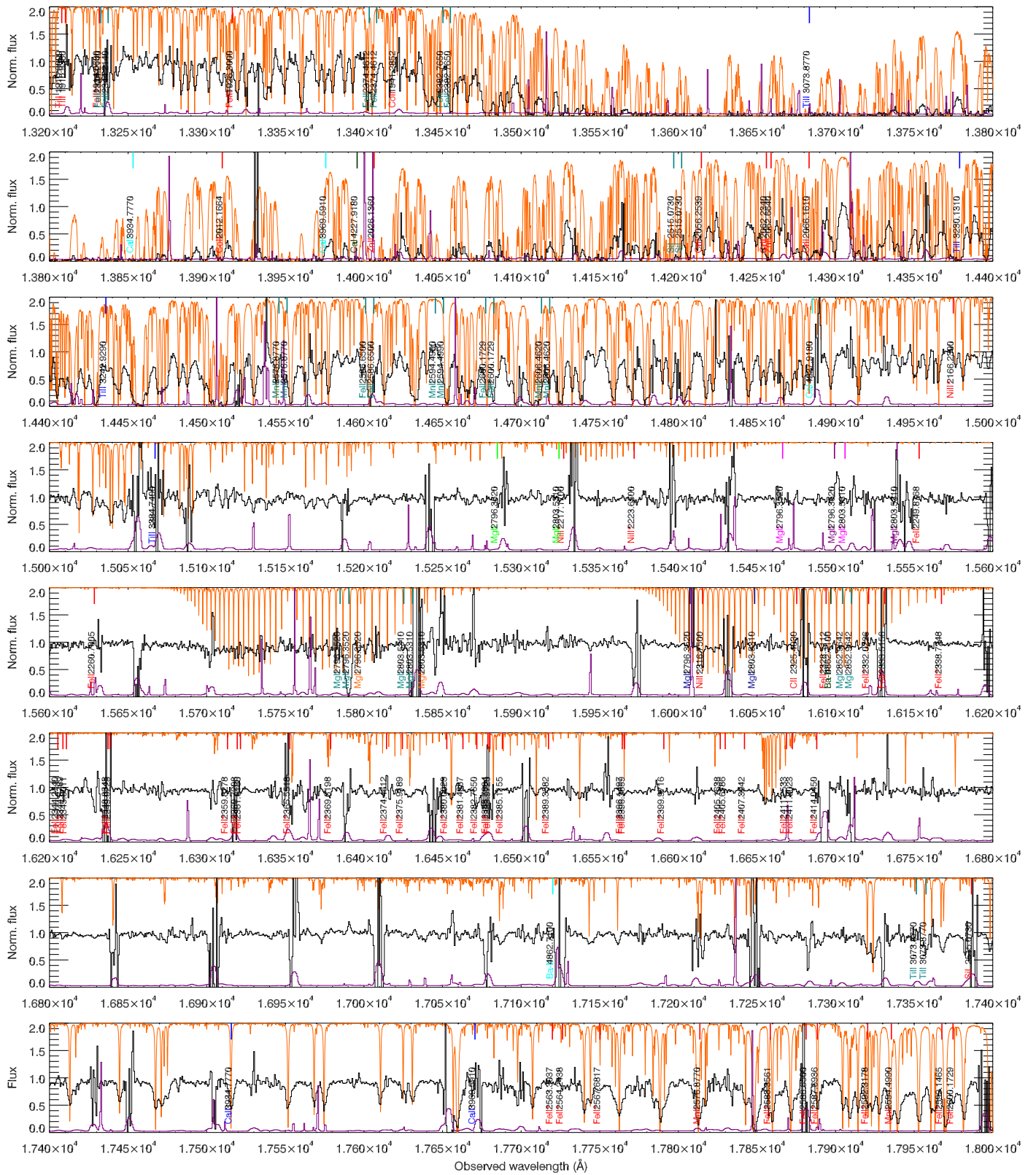


Fig. A.2. Continuation of Figure A.1